Spontaneously promoted osteogenic differentiation of MC3T3-E1 preosteoblasts on ultrathin layers of black phosphorus

Sangheon Jeon [a,1], Jong Ho Lee [b,1], Hee Jeong Jang [a,1], Yu Bin Lee [a], Bongju Kim [c], Moon Sung Kang [a], Yong Cheol Shin [c], Dong-Myeong Shin [d], Suck Won Hong [a,*], Dong-Wook Han [a,e,*]

[a] *Department of Cogno-Mechatronics Engineering, College of Nanoscience & Nanotechnology, Pusan National University, Busan 46241, South Korea*

[b] *Daan Korea Corporation, Seoul 06252, South Korea*

[c] *Dental Life Science Research Institute / Innovation Research & Support Center for Dental Science, Seoul National University Dental Hospital, Seoul 03080, South Korea*

[d] *Department of Biomedical Engineering, The University of Texas at Austin, Austin, TX 78712, USA*

[e] *Department of Mechanical Engineering, The University of Hong Kong, Pokfulam 999077, Hong Kong*

[f] *BIO-IT Foundry Technology Institute, Pusan National University, Busan 46241, South Korea*

* Corresponding authors.

E-mail addresses: swhong@pusan.ac.kr (S.W. Hong), nanohan@pusan.ac.kr (D.-W. Han).

[1] contributed equally to the manuscript.

ABSTRACT

Recently, black phosphorus (BP) has garnered great attention as one of newly emerging two-dimensional nanomaterials. Especially, the degraded platelets of BP in the physiological environment were shown to be nontoxic phosphate anions, which are a component of bone tissue and can be used for mineralization. Here, our study presents the potential of BP as biofunctional and biocompatible nanomaterials for the application to bone tissue engineering and regeneration. An ultrathin layer of BP nanodots (BPNDs) was created on a glass substrate by using a flow-enabled self-assembly process, which yielded a highly uniform deposition of BPNDs in a unique confined geometry. The BPND-coated substrates represented unprecedented favorable topographical microenvironments and supportive matrices suitable for the growth and survival of MC3T3-E1 preosteoblasts. The prepared substrates promoted the spontaneous osteodifferentiation of preosteoblasts, which had been confirmed by determining alkaline phosphatase activity and extracellular calcium deposition as early- and late-stage markers of osteogenic differentiation, respectively. Furthermore, the BPND-coated substrates upregulated the expression of some specific genes (i.e., RUNX2, OCN, OPN, and Vinculin) and proteins, which are closely related to osteogenesis. Conclusively, our BPND-coating strategy suggests that a biologically inert surface can be readily activated as a cell-favorable nanoplatform enabled with excellent biocompatibility and osteogenic ability.

Keywords: Black phosphorus, Flow-enabled self-assembly, Osteogenic differentiation, Bone tissue engineering, Biocompatibility

1. Introduction

The elemental composition on the surface of biomaterials is an important characteristic feature because it exerts a direct and crucial influence on the cellular behaviors in the human body. Several breakthrough advances in tissue engineering have been witnessed to provide biocompatibility and functionality by addressing key challenges for the development of biologically active substrates through extensive surface modification [1-3]. Up to date, numerous types of scaffolds with surface modification have been suggested via the involvement of various nanomaterials to enhance cellular behaviors [4-6]. In particular, nanomaterial-involved substrates can be manufactured using various conventional coating techniques, including spin coating [7,8], dip coating [9-11], drop casting [12,13], vacuum filtration [14], and air-spraying [15], for biomedical applications. However, some of these coating methods produce relatively non-uniform thin films of nanomaterials due to the lack of controllability. Furthermore, it is difficult to obtain large area deposition with the colloidal solutions and a long periodic processing time is required [9,12,14]. One possible technique to overcome the limitations of conventional methods could be the flow-enabled self-assembly (FESA) dragging the sessile droplet in a confined geometry with a precisely controllable manner to deposit colloidal nanomaterials [16,17]. The FESA process can control a micron-scale liquid meniscus of the colloidal solution on a substrate to enable the fabrication of thin-film composed of desired nanomaterials after the solvent evaporation. Especially, the FESA technique has attracted great attention because of the processing simplicity to produce uniformly coated substrates with various types of materials including two-dimensional (2D) nanomaterials [4,18]. In this process, the deposition of 2D nanomaterials can be generated by dynamically dragging the confined meniscus of a colloidal solution in a unique geometry consisted of the angled blade and a substrate, in which the thickness of the initial liquid film

can be tuned by several variables, such as the volume of the colloidal solution, contact angle, and moving speed of the meniscus. In addition, by using this method, 2D nanomaterials can be directly applied to various substrates, such as slide glass, silicon wafers, polymeric films, and metals [4,17-19].

Among other emerging 2D nanomaterials, black phosphorus (BP) has attracted growing interest owing to its intrinsic properties and unique structure [20-23]. In particular, the exceptional attributes of BP, including negligible cytotoxicity, high drug-loading potential, large surface-area-to-volume ratio, and good photoacoustic properties, contribute to its increasing demand in biomedical applications, such as drug delivery, cell imaging, photothermal and photodynamic therapy, and 3D printing [24-27]. BP offers excellent biocompatibility, biodegradability, and biosafety in the body because it is composed of phosphorus (P) elements that comprises the inorganic components of human bone [28-30]. Furthermore, in a physiological environment, BP can be easily oxidized and degraded into nontoxic phosphates and phosphite ions, which implies that it has better biosafety than other 2D nanomaterials [30-32]. In this context, the physicochemical properties in the 2D form of BP can be considered more attractive nanomaterials for bone tissue engineering (BTE) and regeneration, as phosphate is critically important for skeletal development, osteogenesis, and bone regeneration [33-35].

Herein, we developed a simple yet robust strategy to produce a functional substrate for cells using colloidal BP-based nanomaterials via the FESA process and evaluated the cellular behavior of MC3T3-E1 preosteoblasts. In particular, we explored the biocompatibility and spontaneous osteogenic activity of BP nanodots (BPNDs) as a potential candidate for BTE. The colloidal BPND solution was prepared by an exfoliation assisted with a high-intensity ultrasonication, and the nonvolatile solute of BPNDs was uniformly coated on the desired substrate by the FESA process under the controlled solvent evaporation. The physicochemical

properties of the BPNDs and BPND-coated substrates were characterized by transmission electron microscopy (TEM), scanning/transmission electron microscopy (STEM), atomic force microscopy (AFM), Raman spectroscopy, Fourier transform-infrared (FT-IR) spectroscopy, and/or X-ray diffraction (XRD). Moreover, the cellular behaviors of MC3T3-E1 preosteoblasts including proliferation and osteogenic differentiation were extensively evaluated on the BPND-coated substrates. To confirm the positive correlations of the cellular responses according to those nanoscopic surface-mediated cues, mRNA expression levels of some osteogenic markers and their corresponding proteins were investigated by real-time quantitative reverse transcription polymerase chain reaction (qRT-PCR) and immunocytochemistry, respectively. Our results indicate that the BPND-coated substrates promote spontaneous osteogenesis in preosteoblasts cultured on them by providing the nanoscopically favorable surface. These observations, which may have general significance, demonstrate the potential that BPNDs coated on bioinert substrates induce spontaneous osteogenic differentiation in the absence of any osteogenic inducers and growth factors.

2. Experimental

2.1. Preparation and characterizations of BPNDs

A modified ultrasonication-assisted solution method was adopted to prepare BPNDs according to the procedure as described elsewhere [20,36,37]. Briefly, BP (0.4 g, 12.8 mM) was dispersed in deionized (DI) water by high-intensity ultrasound irradiation for 30 min to form several layers of BPNDs and then maintained at room temperature (RT) for 10 min. The supernatant (10 mL) of BP suspension was collected from the dispersion solution, dissolved in DI water, and ultrasonicated for 10 min. These steps were repeated two more times, resulting

in the formation of BPNDs. The morphology and size of the prepared BPNDs were observed by TEM (H-7600, Hitachi, Tokyo, Japan) at an accelerating voltage of 80 kV. Their crystallinity was analyzed by STEM (Talos F200X, FEI, Hillsboro, OR) at an accelerating voltage of 200 kV.

2.2. Preparation and characterizations of BPND-coated substrates

The BPND-coated substrates were produced using the FESA process as described elsewhere [16,19]. Slide glass (25 mm x 75 mm with plain ends and 1.1 – 1.2 mm thickness, Thermo Fisher Scientific, Rockford, IL) was used as the coating substrate. Prior to the deposition process, the substrate was cleaned with a piranha solution (H_2SO_4:H_2O_2 = 2:1) for 2 h, rinsed with DI water, and then dried by blowing with N_2 gas; the hydrophilic surface properties of piranha solution treated substrate naturally induced a complemental wetting of the BPNDs solution with copious hydroxyl groups. A stationary upper blade (2.5 × 7.5 cm^2) was placed on the lower substrate at an angle of 30°, and then a 20 μL droplet of the BPDN solution (10 μg mL^{-1}) was carefully injected in a confined geometry (i.e., between the upper fixed blade and flat glass substrate). The upper blade with carrying capillary-held solution was linearly directed in back-and-forth motion controlled by a motorized stage (AL1–1515–3S, Micro Motion Technology Co., Valley Center, CA) at a constant speed of 20 μm s^{-1}. The optimized deposition number of 100 cycles was performed to coat the surface of the substrates in a sealed chamber to minimized unwanted environmental parameters, maintaining a temperature of 25 ± 2°C, a humidity of 45 ± 1% relative humidity during the evaporative deposition process.

Subsequently, the BPND-coated substrates were completely dried in a vacuum oven at 80°C for 30 min. Finally, the slide glass (25 mm x 75 mm) coated with or without BPNDs was

cut to the desired size (10 mm x 10 mm) using a diamond knife (Diatome AG, Biel, Switzerland).

The surface topography of the BPND-coated substrates was measured by AFM (NX10, Park Systems Co., Suwon, South Korea) in air at RT and image analysis was conducted using XEI Software (version 1.7.1, Park Systems Co.). The compositional analysis of the BPND-coated substrates was characterized by Raman spectroscopy (Micro Raman PL Mapping System, Dongwoo Optron Co., Gwangju, South Korea) and FT-IR spectroscopy (Spectrum GX, PerkinElmer Inc., Waltham, MA). The Raman spectra were obtained using a radially polarized solid-state laser of 532 nm (LasNova 50, Lasos Lasertechnik, Jena, Germany) at a power of 50 mW. The FTIR spectra were recorded in absorption mode over the wavelength range, 500-3500 cm^{-1}, with a resolution of 4.0 cm^{-1} and 16 scans. The crystallinity of the BPNDs coated on the surface of glass substrates was examined by XRD (Empyrean series 2, PANalytical, Almelo, Netherlands) using Cu-Kα radiation (λ = 0.154 nm) at 40 kV and 30 mA. The measurements were conducted over the range, 10–80° 2θ with a scan rate of 2° min^{-1} at RT. Additionally, the water contact angle was measured using a contact angle goniometer (EasyDrop, FM40Mk2, Krüss, Hamburg, Germany) to determine the hydrophilicity of substrates and calculated using a drop-shape analysis program.

2.3. Cell culture and cytotoxicity assay

A murine preosteoblastic cell line (MC3T3-E1 preosteoblasts from C57BL/6 mouse calvaria) was purchased from the American Type Culture Collection (CRL-2593™, ATCC, Rockville, MD). The cells were maintained routinely in a complete α-Minimum Essential Medium (α-MEM) supplemented with 10% (v/v) fetal bovine serum (Sigma-Aldrich Co., St Louis, MO) and a 1% (v/v) antibiotic antimycotic solution (including 10,000 units penicillin,

10 mg streptomycin, and 25 μg amphotericin B per mL, Sigma-Aldrich Co.) at 37°C in a humidified atmosphere of 5% CO_2 in air, which are well known as an established cell line used to examine osteogenesis *in vitro* [38]. α-MEM as basal media (BM) used in the present study did not contain any osteogenic differentiation-inducing factors such as bone morphogenetic protein-2, osteogenin, vitamin D3, β-glycerophosphate, and ascorbate [39,40]. The number of viable cells was indirectly quantified using a cell counting kit-8 (CCK-8, Dojindo, Kumamoto, Japan), which contains a highly water-soluble tetrazolium salt [WST-8, 2-(2-methoxy-4-nitrophenyl)-3-(4-nitrophenyl)-5-(2,4-disulfophenyl)-2*H*-tetrazolium, monosodium salt] reduced to a yellow-color formazan dye by mitochondrial dehydrogenases. Briefly, the CCK-8 assay for the cytotoxicity of BPNDs was conducted as follows: The suspension of MC3T3-E1 preosteoblasts was seeded at a density of 5×10^4 cells/mL in a 96-well plate and then cultured at 37°C in a CO_2 incubator until they were grown as monolayer cultures. Cultured cells were treated with increasing concentrations (0 ~ 250 μg mL^{-1}) of BPNDs and were then incubated with a WST-8 solution for the last 4 h of the culture period (24 and 48 h) at 37°C in the dark. Parallel sets of wells containing freshly cultured non-treated cells were regarded as negative controls. The absorbance was determined at 450 nm using a microplate reader (SpectraMax® 340, Molecular Device Co., Sunnyvale, CA). Relative cell viability was determined as the percentage ratio of the optical density in the medium (containing BPNDs at each concentration) to that in the fresh control medium.

2.4. Cell proliferation assay

For evaluating cell proliferation, MC3T3-E1 preosteoblasts were seeded at a density of 5×10^3 cells/well on either BPND-coated or uncoated substrates and then cultured in the complete media at 37°C in a CO_2 incubator. After 1, 3 and 7 days *in vitro* (DIV) of incubation, the cells

were washed twice with Dulbecco's phosphate-buffered saline (DPBS, Sigma-Aldrich Co.) and then incubated with a WST-8 solution for 4 h at 37°C under a 5% CO_2 atmosphere. To compare the cell proliferation on the BPND-coated substrate with that on the uncoated counterpart, the absorbance was measured at 450 nm using a microplate reader. The cell proliferation profile was determined as the percentage ratio of the optical density in the cells incubated on the BPND-coated substrate at each time point to that on the uncoated control at 1 DIV.

2.5. Alkaline phosphatase (ALP) activity assay

Early-stage osteogenic differentiation was measured using an ALP colorimetric assay kit (Abcam, Cambridge, MA) according to the manufacturer's protocol. MC3T3-E1 preosteoblasts with a density of 2×10^3 cells/well were seeded on either BPND-coated or uncoated substrates and then cultured in a CO_2 incubator. At the end of each pre-determined incubation period (1 to 21 DIV), the cells were washed twice with DPBS and incubated in a 0.1% Triton X-100 solution (Sigma-Aldrich Co.) in Tris-buffer (10 mM, pH 7.5) for 10 min. An 80 μL lysate of each well was mixed with 50 μL of a freshly prepared *ρ*-nitrophenyl phosphate solution and incubated at 37°C in a CO_2 incubator for 1 h. After incubation, 20 μL of a stop solution was added to quench the reaction. *ρ*-Nitrophenol, which is yellow in color, was produced in the presence of ALP and the absorbance was determined at 405 nm using a microplate reader. The absorbance vs. time plot was used to calculate the ALP activity of the cells cultured on the BPND-coated substrate.

2.6. Alizarin red S (ARS) staining

To examine the mineralized nodule formation as a late-stage marker of osteogenic

differentiation, the ARS staining was employed, which is a typical method to monitor the mineralization of the extracellular matrix (ECM) by calcium accumulation [38-40]. Like the ALP activity assay, MC3T3-E1 preosteoblasts were seeded with a density of 2×10^3 cells/well on either BPND-coated or uncoated substrates and then cultured in a CO_2 incubator. After incubation for 1-21 DIV, the cells were washed twice with DPBS, fixed with 70% ethanol for 1 h at 4°C, and then stained with a 40 mM ARS solution (pH 4.2, Sigma-Aldrich Co.) for 10 min at RT. After removing the nonspecific stains by repeated washing with DI water, the cells were observed under an optical microscope (Leica DMIL, Leica Microsystems, Wetzlar, Germany). To quantify ARS staining, ARS in the stained cells was extracted by adding a solution containing 20% (v/v) methanol and 10% (v/v) acetic acid in DI water for 15 min at 37°C. The extracted ARS was quantified by measuring the absorbance at 405 nm using a microplate reader.

2.7. RNA isolation and real-time qRT-PCR

For real-time qRT-PCR analysis, MC3T3-E1 preosteoblasts were cultured on the uncoated and BPND-coated substrates for 14 DIV. Then, the cells were dissociated with 0.05% trypsin-EDTA (Invitrogen, Carlsbad, CA) by mild pipetting. Total RNA was extracted from the detached cells using TRIzol reagent (Invitrogen) and an RNeasy Mini Kit (Qiagen, Grand Island, NY). SuperScript III First-Strand cDNA Synthesis System (Invitrogen) was further used to synthesize first-strand cDNA from total RNA according to the manufacturer's instructions. The mRNA expression of specific genes was then determined by real-time qRT-PCR using the total first-strand cDNA as the template and Power SYBR Green PCR Master Mix (Applied Biosystems, Carlsbad, CA). The sequences of the primers for RUNX2, OCN, OPN, Vinculin, and β-actin are shown in Table S1. The expression level of β-actin was used as an endogenous

normalizer and the relative expression levels were calculated using the $^{-\Delta\Delta Ct}$ method.

2.8. Immunocytochemistry

For osteogenic differentiation analysis with immunofluorescence staining, MC3T3-E1 preosteoblasts were cultured on the uncoated and BPND-coated substrates for 14 DIV. After incubation, the cells were fixed with 4% formaldehyde (Sigma-Aldrich Co.) for 15 min at RT, permeabilized with 0.2% Triton-X 100 for 5 min and then blocked with a 2% bovine serum albumin (GenDEPOT, Barker, TX) solution in DPBS for 30 min. To immunostain osteocalcin (OCN) and osteopontin (OPN), the cells were incubated with primary mouse monoclonal antibody to OCN and rabbit monoclonal antibody to OPN (1:250 and 1:500 dilutions, respectively, Abcam) overnight at 4°C. Subsequently, donkey anti-mouse IgG NorthernLights NL493-conjugated and goat anti-rabbit IgG DyLight488-conjugated secondary antibodies (1:200 dilution each, Abcam) were treated and then reacted with at RT in the dark for 2 h. The nuclei were counterstained with 4′,6-diamidino-2-phenylindole (0.3 μM, DAPI, Sigma-Aldrich Co.) at RT for 30 min. The immunofluorescence images were obtained under a fluorescence (FL) microscope (IX81-F72, Olympus Optical Co., Osaka, Japan) with a digital camera (Olympus Optical Co.). The green FL signals from the micrographs were quantified using ImageJ software (National Institutes of Health, Bethesda, MD) to compare the relative FL intensity of OCN- and OPN-positive areas.

2.9. Statistical analysis

All variables were tested in three independent cultures for each experiment, which was repeated twice (n = 6). The quantitative data is expressed as the mean ± standard deviation

(SD). The data was tested for the homogeneity of the variances using the test of Levene, prior to statistical analysis. Statistical comparisons were carried out using a one-way analysis of variance (ANOVA; SAS Institute Inc., Cary, NC, USA), followed by a Bonferroni test for multiple comparisons. A value of $p < 0.05$ was considered as statistically significant differences among the means.

3. Results and discussion

3.1. Physicochemical properties of BPNDs and BPND-coated substrates

Fig. 1a illustrates the ideal atomic structure of layered BP by the ultrasonication-assisted exfoliation of bulk BP crystals. The Multilayered BP is known to consist of an armchair- and zigzag-shaped honeycomb network along x- and y-direction, respectively. After the ultrasonic exfoliation, the bulk BP was converted to the nanodot suspension monodispersed in the DI water. As shown in Fig. 1b, the TEM observation indicates that the produced BPNDs were uniformly formed in a spherical shape. The atomic arrangement in the crystalline structure displayed the lattice fringe with an interplanar spacing of 0.21 nm (Fig. 1c) that could be assigned to the (002) atomic plane of orthorhombic BP as reported previously [41]. As manually measured, the typical diameter of the BPNDs was distributed to be about 20 to 100 nm, with a mean size of 54.15 ± 19.10 nm (Fig. 1d) as presented in our recent report [37]. The exfoliation of BPNDs is highly reproducible in the firmly established process, which successfully transformed the bulk BP material into well-dispersed nanodot-colloids in an aqueous solution with high stability.

To create a cell-favorable substrate using this BPND colloidal solution, the FESA process

was facilitated as shown in Fig. 2a, which represents a schematic illustration of the confined geometry to trap a droplet solution of BPND, generating uniformly deposited layers of BPND arrays on a glass substrate. The process was started with a careful injection of BPNDs in the confined geometry between the lower glass substrate and an upper fixed blade (~100 μm of distance), trapping a drop of BPND solution (concentration, $C = 10$ μg mL^{-1}) by capillary force. Thus, the capillary-held meniscus could be formed at the liquid-air-solid interface bridged the upper and lower surfaces (right illustration in Fig. 2a). The lower substrate was then driven by a computer-controlled translational stage, repeatedly moving back-and-forth (velocity, $v = 20$ μm s^{-1}) to induce a natural solvent evaporation at the contact line of the meniscus. By this dynamic deposition process, the moving capillary-trapped meniscus uniformly left behind nonvolatile solute (i.e., BPNDs) on the glass substrate as a result of hydrodynamic flow and balanced surface tension at the three-phase contact line. The control of the solvent evaporation was maintained in a sealed chamber to prevent unwanted "*coffee-ring*" effect and the Marangoni flow that usually leads to fractal instabilities in the depositing direction [4,17,19]. Moreover, the travel speed of the translational stage (i.e., deposition speed) was relatively slower than that of the previously reported FESA process to produce uniform nanodot arrays without the formation of a large aggregation reaching a monolayer.[16,19] Because the size deviation of the BPNDs may induce the different nanoscale capillary bridges among the nanodots in the evaporative assembly process, both the control of the deposition speed and the concentration were the main parameter in our experimental system.

The surface topography of thin layer of BPNDs produced through meniscus evaporation control was measured by AFM (Fig. 2b). Unlike a conventional spin coating method, the BPNDs were distributed uniformly over the target substrate. The AFM image of a single BPND revealed a height gradient of ~2-3 nm in the topographic array measured locally with the height profile. In addition, Raman spectroscopy, FT-IR spectroscopy, and XRD were performed to

confirm the chemical composition and crystal structure of the BPND-coated substrate. From the Raman spectra of the BPND-coated substrates (Fig. 2c), the distinct bands were observed at ~365, ~440, and ~470 cm^{-1}, which are attributed to the A_g^1, A_g^2, and B_{2g} modes appearing in phosphorene and are comparable to those of BPNDs [42,43]. The FT-IR spectra showed that the strong peaks at ~1000 cm^{-1} and ~1200 cm^{-1} were assigned to the P–O stretching vibration and P=O linear stretching modes, respectively, whereas the small peak at ~1500 cm^{-1} was assigned to the P=O stretching mode (Fig. 2d). These results were found to be well consistent with those of previous studies [36,44]. The XRD patterns also confirm the orthorhombic crystalline structure of the BPNDs as shown in Fig. 2e, in which the characteristic reflective patterned peaks were observed at 16.9°, 34.2°, 52.3°, and 72.0° of 2θ, corresponding to the d_{020} = 5.2 Å, d_{040} = 2.6 Å, d_{060} = 1.7 Å, and d_{080} = 1.3 Å, respectively [26,42]. The collective set of the physicochemical characteristics indicate that the uniform BPND coatings were successfully generated on a glass substrate by the FESA process. In addition, water contact angle measurement was performed to examine the surface property (Fig. S1). When the same amount of water was dropped onto the uncoated and BPND-coated substrates, the contact angles were 44.2 ± 4.0° and 52.7 ± 6.2°, respectively. Due to the hydrophobic nature of BP [45], the water contact angle of the substrate was apparently increased after BPND coating, but there was no significant difference in the contact angle. Generally, the definition is acceptable that a surface is hydrophobic when its static water contact angle θ is >90° and is hydrophilic when θ is <90° [46]. This result implies that BPND coating of the substrate does not noticeably affect the surface property.

3.2. Proliferation of MC3T3-E1 preosteoblasts on BPND-coated substrates

Before examining the cell growth on the uncoated and BPND-coated substrates, the

cytotoxicity of BPNDs against MC3T3-E1 preosteoblasts had been determined. Cells were treated with increasing concentrations (0 - 250 μg mL^{-1}) of BPNDs for 24 and 48 h and then the viability was measured using a CCK-8 assay. After 24 h of exposure to 62.5 μg mL^{-1} of BPNDs, the cell viability significantly decreased to approximately 42% (Fig. S2a). On the other hand, the cells were all viable at the concentrations lower than 31 μg mL^{-1}. After 48 h, the cytotoxicity of BPNDs was negligible at the concentrations lower than 4 μg mL^{-1}. However, only about 44% cells were found to be viable even at 16 μg mL^{-1} (Fig. S2b). This result implies that the cell viability has a tendency to decrease as an incubation time increases. Although the cytotoxicity of BP may differ depending on the BP size and dose, measurement methods, and cell types, BP nanoparticles (NPs) generally show dose-dependent cytotoxicity, but they have no significant cytotoxic effects against the cells at relatively low concentrations of 4 μg mL^{-1} as reported previously [47,48]. It could be also confirmed by the morphological changes of MC3T3-E1 preosteoblasts treated with BPNDs (Fig. S2c). Any morphological alterations were not observed after 24 and 48 h of incubation as well at relatively low concentrations of BPNDs i.e., $\leq$ 4 μg mL^{-1}), which would not adversely affect the cell growth and survival and allow cells to interact favorably with BPNDs. In our previous studies, it was confirmed that BPNDs showed increasing cytotoxicity in dose- and time-dependent manners, which attributes to oxidative stress and subsequent membrane destruction by BP NPs [36,44,49].

Despite of the great biological potential of BPNDs, their biosafety and stability issues still remain to be unraveled. It was reported that intravenously injected BP NPs were mainly accumulated in the reticuloendothelial system organs and that their degradation and clearance occurred via hepatobiliary excretion and kidney after having 9.47 h of blood circulation [50]. Furthermore, BP NPs were shown to trigger inflammatory response by activating NF-κB signaling pathway and to induce immunotoxicity and immune perturbation in macrophages [51,52]. To dispel such concerns, some scholars have pointed out that while bare BP NPs may

have a potential inflammatory response, they can efficiently escape from macrophages uptake, and reduce the cytotoxicity and proinflammation when modified with titanium sulfonate ligand [53]. On the other hand, a recent study has revealed that fewer-layer BP nanosheets are more prone to react with water and oxygen, and are more easily degraded. The poor stability of BP under the conditions of water and oxygen will limit its practical application. To improve the stability of BP, some useful ways has been widely employed such as adding protective layer, surface chemical modification, and physical mixture [30,54].

These studies imply necessity of rational design of BPNDs for potential application and further investigation on their potential side effect need to be conducted.

To assess the proliferation pattern, MC3T3-E1 preosteoblasts were cultured on the uncoated and BPND-coated substrates for 1, 3, and 7 DIV. As shown in Fig. 3a, the cells on each substrate represent a normally proliferating tendency during the culture period. The proliferation rate on the BPND-coated substrates was noticeably changed at 3 DIV and increased approximately 6.4-fold compared to that at 1 DIV, which is considered to be mediated by the positive effect of BP on cell proliferation via the supply of phosphate at a high extracellular concentration [37,55]. However, there was no significant difference in the proliferation ratio between the uncoated and BPND-coated substrates. Consequently, it is suggested that the BPND-incorporated substrates and matrices can provide favorable microenvironments and supportive matrices suitable for the cell growth and survival [56,57]. This result well agreed with the morphological observation. As shown in Fig. 3b, MC3T3-E1 preosteoblasts cultured on the BPND-coated substrates exhibited normal cellular morphologies, which means that the cells maintain the capability to normally metabolize, proliferate, migrate, and spread out on them following adhesion to them. This phenomenon can be explained partly by the previous study report that the small-sized (< 200 nm) BP NPs do not interfere with the cell proliferation [49,58]. Hence, the BPNDs prepared in this study did not negatively affect

the cell proliferation, as their average size was less than 60 nm (Fig. 1d)

3.3. Osteodifferentiation of MC3T3-E1 preosteoblasts on BPND-coated substrates

The osteogenic differentiation of MC3T3-E1 preosteoblasts on the BPND-coated substrates was examined using two typical osteogenic markers, ALP activity and extracellular calcium deposition. Figure 4 shows the ALP activity of the cells on the uncoated and BPND-coated substrates. The ALP activity has been used extensively as an early osteodifferentiation marker and is strongly related to the mineralization capability of osteoblasts [38-40]. Osteoblastic cells mostly proliferate for approximately 7 DIV, and then begin secreting ECM proteins followed by producing ALP [59]. At 7 DIV, the ALP activity of MC3T3-E1 preosteoblasts on the BPND-coated substrates showed a similar level to that on the uncoated ones. On the contrary, the cells cultured on the BPND-coated substrates for 14 and 21 DIV showed significant ($p < 0.05$) increases in the ALP activity compared to those cultured on the uncoated counterparts. ALP is the main marker that reflects bone metabolic capacity, and its level is closely related to the differentiation of osteoblasts and greatly affects the process of matrix mineralization [38-40]. These findings suggest that the BPND-coated substrates can enhance the early marker of osteogenic differentiation without any osteogenic factors.

For ALP activity analysis under osteogenic conditions, MC3T3-E1 preosteoblasts on either BPND-coated or uncoated substrates were incubated in osteoinduction media (OIM) based on BM containing osteogenesis-inducing factors such as 10 mM β-glycerophosphate, 10 nM dexamethasone, and 50 mM L-ascorbic acid for up to 21 DIV, and then their ALP activity was measured. The cells cultured in OIM for 7 DIV showed remarkably higher ALP activity (>58 nmol/mL/min, Fig. S3) than those cultured in basal media (~33 nmol/mL/min, Fig. 4), irrespective of BPND coating. Even at 21 DIV, the ALP activity of the cells on the uncoated

and BPND-coated substrates in OIM reached about 2.5 and 1.6 times the values in BM, respectively. These results indicate that when cultured in OIM, the osteogenic differentiation of preosteoblasts on the BPND-coated substrate can be synergistically induced. Although there were synergistic effects, statistically significant results were observed to induce osteodifferentiation only by culturing the cells on the BPND-coated substrate without adding such osteoinductive factors.

In addition to the ALP activity, mineralized calcium nodules in the cells stained with ARS were extracted and analyzed quantitatively on the uncoated and BPND-coated substrates. Figure 5a shows optical microscopic images of the ARS-stained cells on both the substrates. Since a high intensity of ARS staining indicates higher calcium concentration, the micrographs of the BPND-coated substrates clearly reveal the highest level of calcium deposition at 21 DIV. These qualitative image data were further confirmed by the quantitative analysis to show the absorbance of ARS extracted from the stained calcium deposits (Fig. 5b) [55,59]. As a result, it was found that the BPND-coated substrates could significantly ($p < 0.05$) increase extracellular calcium deposition and mineralization in MC3T3-E1 osteoblasts after 14 DIV.

3.4. Expression of osteogenesis genes in MC3T3-E1 preosteoblasts on BPND-coated substrates

To explore the underlying mechanism for the spontaneously promoted osteodifferentiation of MC3T3-E1 preosteoblasts on the BPND-coated substrates, the expression levels of osteogenesis-related genes such as RUNX2, OCN, OPN, and Vinculin were thoroughly examined using real-time qRT-PCR. The cells were seeded on the uncoated and BPND-coated substrates, and then cultured for 14 DIV. As shown in Fig. 6, regarding the mRNA expression levels of the four established osteogenic differentiation markers, the presence of the BPND

arrays in the ultrathin film significantly ($p < 0.05$) upregulated the mRNA expression of all the osteogenic markers compared to that on the uncoated substrates. OCN, also known as bone gamma-carboxyglutamic acid-containing protein (BGLAP), was first identified as a calcium-binding protein and frequently used as a marker for the bone formation process as it is secreted solely by osteoblasts [60]. The cells cultured on the BPND-coated substrates indicated significantly ($p < 0.05$) increased mRNA expression of OCN around 5.39-fold higher than those cultured on the uncoated counterparts. OPN, bone sialoprotein I (BSP-1), is a highly negatively charged protein component of extracellular matrix that allows binding strongly to various types of calcium-based biominerals in bones and teeth, so thus its identification is important [61,62]. Significant ($p < 0.05$) upregulation of OPN expression was found up to ~7.81-fold on the BPND-coated substrates directly, compared to the uncoated control. For further validation of osteogenesis, the mRNA expression of RUNX2 and Vinculin was quantified, and significantly ($p < 0.05$) increased expressions were also shown in the cells cultured on the BPND-coated substrates at 14 DIV. As well known, RUNX2 is a key transcription factor associated with early osteoblast differentiation as the master gene of bone formation, but not essential for the late-stage of osteoblast differentiation [63]. However, Vinculin is a ubiquitously expressed actin-binding protein frequently used as a marker for both focal adhesion and adherens junctions [64]. Therefore, as the increased expression of those genes might regulate mineralization and transcription simultaneously in preosteoblasts on the BPND-mediated bioactive surfaces, we postulate that the spontaneous osteodifferentiation can be attributed to the proteins expressed by these genes.

3.5. Expression of osteogenesis proteins in MC3T3-E1 preosteoblasts on BPND-coated substrates

In addition to the earlier evaluation, immunofluorescence analysis was performed to

investigate the expression of OCN and OPN proteins, which are associated with matrix maturation and calcification as the late-stage markers for osteodifferentiation [65]. Immunofluorescence staining for OCN and OPN demonstrates that the BPND-coated substrates appreciably upregulated the expression of OCN and OPN in MC3T3-E1 preosteoblasts at 14 DIV of incubation in BM without any osteogenic factors (Fig. 7a and 7b). In contrast, uncoated substrates showed a relatively lower expression of OCN and OPN. The merged images (M2) of nucleus (Nu) and OCN or OPN with phase contrast (PC) one showed a clearer difference between the uncoated and BPND-coated substrates. These observations were confirmed by the relative FL intensity to show that the green FL signals from the micrographs of the BPND-coated substrates were significantly ($p < 0.05$) higher than those of the uncoated counterparts (Fig. 7c). This set of results fully agreed with that of qPT-PCR (Fig. 6) and implied that the BPND-coated substrates possess the remarkable potential to promote the spontaneous osteogenic differentiation of preosteoblasts. Crucially, the dense nanoscale array of the BPNDs on the substrates sufficiently supplied phosphorus to the cells, leading to an optimal environment for osteodifferentiation [30,32]. Indeed, the BPND-involved cell culture platform was simply developed to improve the surface-mediated bioactivity of nanomaterials, expressing unprecedented osteodifferentiation and matrix mineralization. We believe that the presented BPNDs would be potential candidates for promising scaffolds in BTE, stimulators for osteogenic differentiation of stem cells, and components of implantable devices, due to their biocompatible and bioactive properties.

4. Conclusions

Although BPND-coated substrates have achieved satisfactory results in promotion of spontaneous osteogenic differentiation, the research on BP in the biomedical fields is still in its infancy [66]. For future clinical applications of BPNDs, there are challenges to be overcome,

such as poor stability, difficulty to store for a long time, and cumbersome preparation [30]. Additionally, in vivo availability of BPNDs, including biodistribution and accumulation as well as unclear mechanisms for immune reaction and inflammatory responses should be clearly elucidated by multifaceted studies, which can help reduce their side effects and maximize their biosafety and efficacy.

Herein, we developed a robust strategy to fabricate a bioactive substrate utilizing BPND colloids with easy access to determine whether it is beneficial to osteogenic differentiation for potential applications to BTE. The BPND-coated substrates were fabricated using the FESA process, yielding a spatially uniform distribution in the structure. MC3T3-E1 preosteoblasts cultured on the BPND-coated substrates did not show any retardation in their growth, but rather slightly increased their proliferation. Furthermore, these cytocompatible BPND-coated substrates exhibited osteogenic activity to induce the spontaneous osteodifferentiation of preosteoblasts by providing a suitable topographical environment for osteogenesis. This phenomenon was firstly proved by significantly elevated osteogenic markers such as ALP activity and calcium deposition. The BPND-coated substrates upregulated the expression of representative genes (i.e., RUNX2, OCN, OSX, and OPN) and proteins (i.e., OCN and OPN) regarding osteogenesis. However, the more detailed mechanisms involved in intracellular signaling pathways are still ambiguous and require further study at molecular levels. We envision that the remarkable potential to spontaneously stimulate osteogenesis by activating cell-favorable surfaces via a BPND-based biointerface allows us to craft a broad range of strategies for the surface functionalization of dental and orthopedic implants.

Acknowledgments

519 This work was supported by the National Research Foundation of Korea (NRF) grant
520 funded by the Korea government (MSIT) (No. 2019R1A4A1024116, 2020R1F1A1077033 and
521 2021R1A2C2006013).
522

523 ## Refenrences

524 [1] Y.C. Shin, S.-J. Song, S.W. Hong, S.J. Jeong, W. Chrzanowski, J.-C. Lee, D.-W. Han,
525 Multifaceted biomedical applications of functional graphene nanomaterials to coated
526 substrates, patterned arrays and hybrid scaffolds, Nanomaterials 7 (11) (2017) 369.
527 [2] Y.C. Shin, K.-M. Pang, D.-W. Han, K.-H. Lee, Y.-C. Ha, J.-W. Park, B. Kim, D. Kim,
528 J.-H. Lee, Enhanced osteogenic differentiation of human mesenchymal stem cells on Ti
529 surfaces with electrochemical nanopattern formation, Mater. Sci. Eng. C 99 (2019)
530 1174-1182.
531 [3] J. Quinn, R. McFadden, C.W. Chan, L. Carson, Titanium for orthopedic applications:
532 an overview of surface modification to improve biocompatibility and prevent bacterial
533 biofilm formation, iScience 23 (11) (2020) 101745.
534 [4] K.O. Park, J.H. Lee, J.H. Park, Y.C. Shin, J.B. Huh, J.H. Bae, S.H. Kang, S.W. Hong,
535 B. Kim, D.J. Yang, D.-W. Han, J.H. Yeum, Graphene oxide-coated guided bone
536 regeneration membranes with enhanced osteogenesis: spectroscopic analysis and
537 animal study, Appl. Spectrosc. Rev. 51 (7-9) (2016) 540-551.
538 [5] Y.C. Shin, J. Kim, S.E. Kim, S.-J. Song, S.W. Hong, J.-W. Oh, J. Lee, J.-C. Park, S.-H.
539 Hyon, D.-W. Han, RGD peptide and graphene oxide co-functionalized PLGA nanofiber
540 scaffolds for vascular tissue engineering, Regen. Biomater. 4 (3) (2017) 159-166.
541 [6] M.S. Kang, J.H. Lee, S.-J. Song, D.-M. Shin, J.-H. Jang, S.-H. Hyon, S.W. Hong, J.H.
542 Lee, D.-W. Han. Graphene oxide-functionalized nanofibre composite matrices to

enhance differentiation of hippocampal neuronal cells. Mater. Adv. 1 (9) (2020) 3496-3506.

[7] Q. Yu, Y. Han, T. Tian, Q. Zhou, Z. Yi, J. Chang, C. Wu, Chinese sesame stick-inspired nano-fibrous scaffolds for tumor therapy and skin tissue reconstruction, Biomaterials 194 (2019) 25-35.

[8] N.D. Montañez, H. Carreno, P. Escobar, H.A. Estupinan, D.Y. Pena, S. Goel, J.L. Endrino, Functional evaluation and testing of a newly developed Teleost's Fish Otolith derived biocomposite coating for healthcare, Sci. Rep. 10 (1) (2020) 258.

[9] Y.C. Shin, S.H. Kang, J.H. Lee, B. Kim, S.W. Hong, D.-W. Han, Three-dimensional graphene oxide-coated polyurethane foams beneficial to myogenesis, J. Biomater. Sci. Polym. Ed. 29 (7-9) (2018) 762-774.

[10] A.D. Holmkvist, J. Agorelius, M. Forni, U.J. Nilsson, C.E. Linsmeier, J. Schouenborg, Local delivery of minocycline-loaded PLGA nanoparticles from gelatin-coated neural implants attenuates acute brain tissue responses in mice, J. Nanobiotechnology 18 (1) (2020) 27.

[11] I. Borges, P.C. Henriques, R.N. Gomes, A.M. Pinto, M. Pestana, F.D. Magalhaes, I.C. Goncalves, Exposure of smaller and oxidized graphene on polyurethane surface improves its antimicrobial performance, Nanomaterials 10 (2) (2020) 349.

[12] J.H. Lee, Y.C. Shin, O.S. Jin, D.-W. Han, S.H. Kang, S.W. Hong, J. M. Kim, Enhanced neurite outgrowth of PC-12 cells on graphene-monolayer-coated substrates as biomimetic cues, J. Korean Phys. Soc. 61 (10) (2012) 1696-1699.

[13] B. Cai, L. Huang, H. Zhang, Z. Sun, Z. Zhang, G. Zhang, Gold nanoparticles-decorated graphene field-effect transistor biosensor for femtomolar MicroRNA detection, Biosens. Bioelectron. 74 (2015) 329-334.

[14] B. Liang, L. Fang, Y. Hu, G. Yang, Q. Zhu, X. Ye, Fabrication and application of flexible graphene silk composite film electrodes decorated with spiky Pt nanospheres, Nanoscale 6 (8) (2014) 4264-4274.

[15] H. Chen, J. Shen, L. Guo, Y. Chen, D.-H. Kim, Cellular response of RAW 264.7 to spray-coated multi-walled carbon nanotube films with various surfactants, J. Biomed. Mater. Res. A 96 (2) (2011) 413-421.

[16] S.H. Kang, W.S. Hwang, Z. Lin, S.H. Kwon, S.W. Hong, A robust highly aligned DNA nanowire array-enabled lithography for graphene nanoribbon transistors, Nano Lett. 15 (12) (2015) 7913-7920.

[17] D.G. Bae, J.-E. Jeong, S.H. Kang, M. Byun, D.-W. Han, Z. Lin, H.Y. Woo, S.W. Hong, A nonconventional approach to patterned nanoarrays of DNA strands for template-assisted assembly of polyfluorene nanowires, Small 12 (31) (2016) 4254-4263.

[18] S. Jeon, J. Lee, R. Park, J. Jeong, M.C. Shin, S.U. Eom, J. Park, S.W. Hong, Graphene templated DNA arrays and biotin-streptavidin sensitive bio-transistors patterned by dynamic self-assembly of polymeric films confined within a roll-on-plate geometry, Nanomaterials 10 (8) (2020) 1468.

[19] R. Park, H. Kim, S. Lone, S. Jeon, Y.W. Kwon, B. Shin, S.W. Hong, One-step laser patterned highly uniform reduced graphene oxide thin films for circuit-enabled tattoo and flexible humidity sensor application, Sensors 18 (6) (2018) 1857.

[20] H.U. Lee, S.Y. Park, S.C. Lee, S. Choi, S. Seo, H. Kim, J. Won, K. Choi, K.S. Kang, H.G. Park, H.S. Kim, H.R. An, K.H. Jeong, Y.C. Lee, J. Lee, Black phosphorus (BP) nanodots for potential biomedical applications, Small 12 (2) (2016) 214-219.

[21] M. Qiu, W. Ren, T. Jeong, M. Won, G. Park, D. Sang, L. Liu, H. Zhang, J.S. Kim, Omnipotent phosphorene: a next-generation, two-dimensional nanoplatform for multidisciplinary biomedical applications, Chem. Soc. Rev. 47 (15) (2018) 5588-5601.

592 [22] G. Zeng, Y. Chen, Surface modification of black phosphorus-based nanomaterials in
593 biomedical applications: strategies and recent advances, Acta Biomater. 118 (2020) 1-
594 17.
595 [23] L. He, X. Zhou, W. Cai, Y. Xiao, F. Chu, X. Mu, X. Fu, Y. Hu, L. Song, Electrochemical
596 exfoliation and functionalization of black phosphorene to enhance mechanical
597 properties and flame retardancy of waterborne polyurethane, Compos. B Eng. 202
598 (2020) 108446.
599 [24] Y. Li, Z. Liu, Y. Hou, G. Yang, X. Fei, H. Zhao, Y. Guo, C. Su, Z. Wang, H. Zhong, Z.
600 Zhuang, Z. Guo, Multifunctional nanoplatform based on black phosphorus quantum
601 dots for bioimaging and photodynamic/photothermal synergistic cancer therapy, ACS
602 Appl. Mater. Interfaces 9 (30) (2017) 25098-25106.
603 [25] J.R. Choi, K.W. Yong, J.Y. Choi, A. Nilghaz, Y. Lin, J. Xu, X. Lu, Black phosphorus
604 and its biomedical applications, Theranostics 8 (4) (2018) 1005-1026.
605 [26] Y.C. Shin, S.J. Song, Y.B. Lee, M.S. Kang, H.U. Lee, J.-W. Oh, D.-W. Han, Application
606 of black phosphorus nanodots to live cell imaging, Biomater. Res. 22 (2018) 31.
607 [27] C. Wang, X. Ye, Y. Zhao, L. Bai, Z. He, Q. Tong, X. Xie, H. Zhu, D. Cai, Y. Zhou, B.
608 Lu, Y. Wei, L. Mei, D. Xie, M. Wang, Cryogenic 3D printing of porous scaffolds for in
609 situ delivery of 2D black phosphorus nanosheets, doxorubicin hydrochloride and
610 osteogenic peptide for treating tumor resection-induced bone defects, Biofabrication 12
611 (3) (2020) 035004.
612 [28] B. Yang, J. Yin, Y. Chen, S. Pan, H. Yao, Y. Gao, J. Shi, 2D-Black-phosphorus-
613 reinforced 3D-printed scaffolds: a stepwise countermeasure for osteosarcoma, Adv.
614 Mater. 30 (10) (2018) 1705611.
615 [29] . Luo, T. Fan, Y. Zhou, H. Zhang, L. Mei, 2D black phosphorus–based biomedical
616 applications, Adv. Func. Mater. 29 (13) (2019) 1808306.

[30] L. Cheng, Z.W. Cai, J.W. Zhao, F. Wang, M. Lu, L.F. Deng, W.G. Cui, Black phosphorus-based 2D materials for bone therapy, Bioact. Mater. 5 (4) (2020) 1026-1043.

[31] H. Wang, L. Zhong, Y. Liu, X. Xu, C. Xing, M. Wang, S.-M. Bai, C.-H. Lu, H.-H. Yang, A black phosphorus nanosheet-based siRNA delivery system for synergistic photothermal and gene therapy, Chem. Commun. 54 (25) (2018) 3142-3145.

[32] M. van Druenen, Degradation of black phosphorus and strategies to enhance its ambient lifetime, Adv. Mater. Interfaces 7 (22) (2020) 2001102.

[33] J. Jeong, J.H. Kim, J.H. Shim, N.S. Hwang, C.Y. Heo, Bioactive calcium phosphate materials and applications in bone regeneration, Biomater. Res. 23 (2019) 4.

[34] T. Michigami, K. Ozono, Roles of phosphate in skeleton, Front. Endocrinol. 10 (2019) 180.

[35] L. Cheng, Z. Chen, Z. Cai, J. Zhao, M. Lu, J. Liang, F. Wang, J. Qi, W. Cui, L. Deng, Bioinspired functional black phosphorus electrospun fibers achieving recruitment and biomineralization for staged bone regeneration, Small 16 (50) (2020) 2005433.

[36] S.-J. Song, I.S. Raja, Y.B. Lee, M.S. Kang, H.J. Seo, H.U. Lee, D.-W. Han, Comparison of cytotoxicity of black phosphorus nanosheets in different types of fibroblast, Biomater. Res. 23 (2019) 23.

[37] M.S. Kang, S.-J. Song, J.H. Cha, Y. Cho, H.U. Lee, S.-H. Hyon, J.H. Lee, D.-W. Han, Increased neuritogenesis on ternary nanofiber matrices of PLCL and laminin decorated with black phosphorus, J. Ind. Eng. Chem. 92 (2020) 226-235.

[38] Y.C. Shin, J.H. Lee, O.S. Jin, S.H. Kang, S.W. Hong, B. Kim, J.-C. Park, D.-W. Han, Synergistic effects of reduced graphene oxide and hydroxyapatite on osteogenic differentiation of MC3T3-E1 preosteoblasts, Carbon 95 (2015) 1051-1060.

[39] J.H. Lee, Y.C. Shin, S.M. Lee, O.S. Jin, S.H. Kang, S.W. Hong, C.-M. Jeong, J.B. Huh, D.-W. Han, Enhanced osteogenesis by reduced graphene oxide/hydroxyapatite nanocomposites, Sci. Rep. 5 (2015) 18833.

[40] J.H. Lee, Y.C. Shin, O.S. Jin, S.H. Kang, Y.-S. Hwang, J.-C. Park, S.W. Hong, D.-W. Han, Reduced graphene oxide-coated hydroxyapatite composites stimulate spontaneous osteogenic differentiation of human mesenchymal stem cells, Nanoscale 7 (27) (2015) 11642-11651.

[41] A.R. Baboukani, I. Khakpour, V. Drozd, A. Allagui, C. Wang, Single-step exfoliation of black phosphorus and deposition of phosphorene via bipolar electrochemistry for capacitive energy storage application, J. Mater. Chem. A 7 (44) (2019) 25548-25556.

[42] S. Seo, H.U. Lee, S.C. Lee, Y. Kim, H. Kim, J. Bang, J. Won, Y. Kim, B. Park, J. Lee, Triangular black phosphorus atomic layers by liquid exfoliation, Sci. Rep. 6 (2016) 23736.

[43] Z. Hu, T. Niu, R. Guo, J. Zhang, M. Lai, J. He, L. Wang, W. Chen, Two-dimensional black phosphorus: its fabrication, functionalization and applications, Nanoscale 10 (46) (2018) 21575-21603.

[44] S.-J. Song, Y.C. Shin, H.U. Lee, B. Kim, D.-W. Han, D. Lim, Dose- and time-dependent cytotoxicity of layered black phosphorus in fibroblastic cells, Nanomaterials 8 (6) (2018) 408.

[45] Y. Huang, J. Qiao, K. He, S. Bliznakov, E. Sutter, X. Chen, D. Luo, F. Meng, D. Su, J. Decker, W. Ji, R. S. Ruoff, P. Sutter, Interaction of black phosphorus with oxygen and water, Chem. Mater. 28 (22) (2016) 8330-8339.

[46] K.-Y. Law, Definitions for hydrophilicity, hydrophobicity, and superhydrophobicity: getting the basics right, J. Phys. Chem. Lett. 5 (4) (2014) 686-688.

[47] X. Mu, J.-Y. Wang, X. Bai, F. Xu, H. Liu, J. Yang, Y. Jing, L. Liu, X. Xue, H. Dai, Q. Liu, Y.-M. Sun, C. Liu, X.-D. Zhang, Black phosphorus quantum dot induced oxidative stress and toxicity in living cells and mice, ACS Appl. Mater. Interfaces 9 (24) (2017) 20399-20409.

[48] F. Ruan, R. Liu, K. Wang, J. Zeng, Z. Zuo, C. He, Y. Zhang, Cytotoxicity of black phosphorus quantum dots on lung-derived cells and the underlying mechanisms, J. Hazard. Mater. 402 (2021) 122875.

[49] Y.B. Lee, S.-J. Song, Y.C. Shin, Y.J. Jung, B. Kim, M.S. Kang, I.K. Kwon, S.-H. Hyon, H.U. Lee, S.-H. Jung, D. Lim, D.-W. Han, Ternary nanofiber matrices composed of PCL/black phosphorus/collagen to enhance osteodifferentiation, J. Ind. Eng. Chem. 80 (2019) 802-810.

[50] C. Sun, Y. Xu, L. Deng, H. Zhang, Q. Sun, C. Zhao, Z. Li, Blood circulation, biodistribution, and pharmacokinetics of dextran-modified black phosphorus nanoparticles, Appl. Mater. Interfaces 1 (3) (2018) 673-682.

[51] H. Qin, J. Chen. Y. Lia, L. Gao, J. Wang, G. Qu, M. Yang, X. Zhou, Z. Sun, Inflammatory response induced by black phosphorus nanosheets in mice and macrophages, Sci. Total Environ. 782 (2021) 146860.

[52] J. Mo, Q. Xie, W. Wei, J. Zhao, Revealing the immune perturbation of black phosphorus nanomaterials to macrophages by understanding the protein corona, Nat. Commun. 9 (1) (2018) 2480-2491.

[53] G. Qu, W. Liu, Y. Zhao, J. Gao, T. Xia, J. Shi, L. Hu, W. Zhou, J. Gao, H. Wang, Q. Luo, Q. Zhou, S. Liu, X.F. Yu, G. Jiang, Improved biocompatibility of black phosphorus nanosheets by chemical modification, Angew. Chem. Int. Ed. 56 (46) (2017) 14488-14493.

[54] R. Gusmão, Z. Sofer, M. Pumera, Functional protection of exfoliated black phosphorus by noncovalent modification with anthraquinone, ACS Nano 12 (6) (2018) 5666-5673.

[55] K. Huang, J. Wu, Z. Gu, Black phosphorus hydrogel scaffolds enhance bone regeneration via a sustained supply of calcium-free phosphorus, ACS Appl. Mater. Interfaces 11 (3) (2019) 2908-2916.

[56] Y.L. Miao, X. Shi, Q. Li, L. Hao, L. Liu, X. Liu, Y. Chen, Y. Wang, Engineering natural matrices with black phosphorus nanosheets to generate multi-functional therapeutic nanocomposite hydrogels, Biomater. Sci. 7 (10) (2019) 4046-4059.

[57] Y. Qing, R. Li, S. Li, Y. Li, X. Wang, Y. Qin, Advanced black phosphorus nanomaterials for bone regeneration, Int. J. Nanomedicine 15 (2020) 2045-2058.

[58] X. Zhang, Z. Zhang, S. Zhang, D. Li, W. Ma, C. Ma, F. Wu, Q. Zhao, Q. Yan, B. Xing, Size effect on the cytotoxicity of layered black phosphorus and underlying mechanisms, Small 13 (32) (2017) 1701210.

[59] M.G. Raucci, I. Fasolino, M. Caporali, M. Serrano-Ruiz, A. Soriente, M. Peruzzini, L. Ambrosio, Exfoliated black phosphorus promotes in vitro bone regeneration and suppresses osteosarcoma progression through cancer-related inflammation inhibition, ACS Appl. Mater. Interfaces 11 (9) (2019) 9333-9342.

[60] S.C. Moser, B.C.J. van der Eerden, Osteocalcin-a versatile bone-derived hormone, Front. Endocrinol. 9 (2019) 794.

[61] M.A. Icer, M. Gezmen-Karadag, The multiple functions and mechanisms of osteopontin, Clin. Biochem. 59 (2018) 17-24.

[62] T. Iline-Vul, R. Nanda, B. Mateos, S. Hazan, I. Matlahov, I. Perelshtein, K. Keinan-Adamsky, G. Althoff-Ospelt, R. Konrat, G. Goobes, Osteopontin regulates biomimetic calcium phosphate crystallization from disordered mineral layers covering apatite crystallites, Sci. Rep. 10 (1) (2020) 15722.

713 [63] T.M. Liu, E.H. Lee, Transcriptional regulatory cascades in Runx2-dependent bone
714 development, Tissue Eng. Part B Rev. 19 (3) (2013) 254-263.
715 [64] W.H. Ziegler, R.C. Liddington, D.R. Critchley, The structure and regulation of vinculin,
716 Trends Cell. Biol. 16 (9) (2006) 453-460.
717 [65] M. Yang, J. Wang, Y. Zhu, C. Mao, Bio-templated growth of bone minerals from
718 modified simulated body fluid on nanofibrous decellularized natural tissues, J. Biomed.
719 Nanotechnol. 12 (4) (2016) 753-761.
720 [66] S. Anju, J. Ashtami, P.V. Mohanan, Black phosphorus, a prospective graphene substitute
721 for biomedical applications, Mater. Sci. Eng. C 97 (2019) 978-993.
722

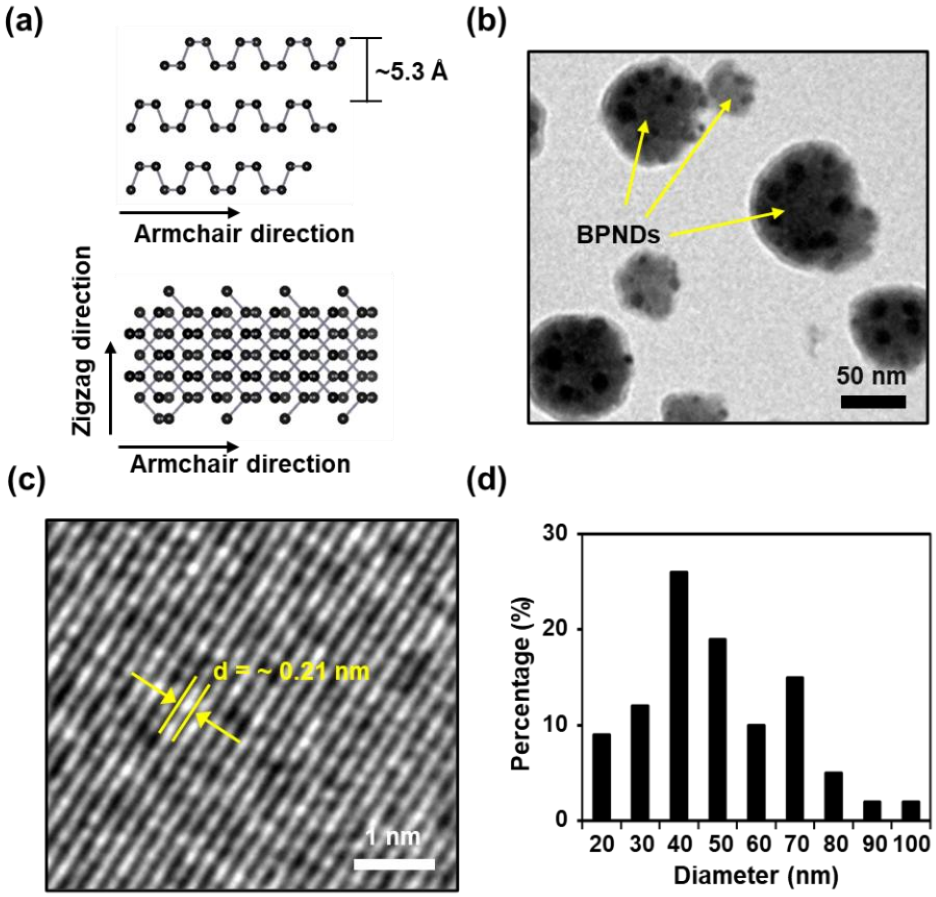

723

724 **Figure 1.** Characterization of the BPNDs. (a) General atomic structure of few-layered BP. (b)
725 TEM image of BPNDs prepared by the ultrasonication-assisted exfoliation. (c) Crystalline
726 structure of the BPND measured by HRTEM. (d) Statistical size distribution of BPNDs
727 measured from TEM images.

728

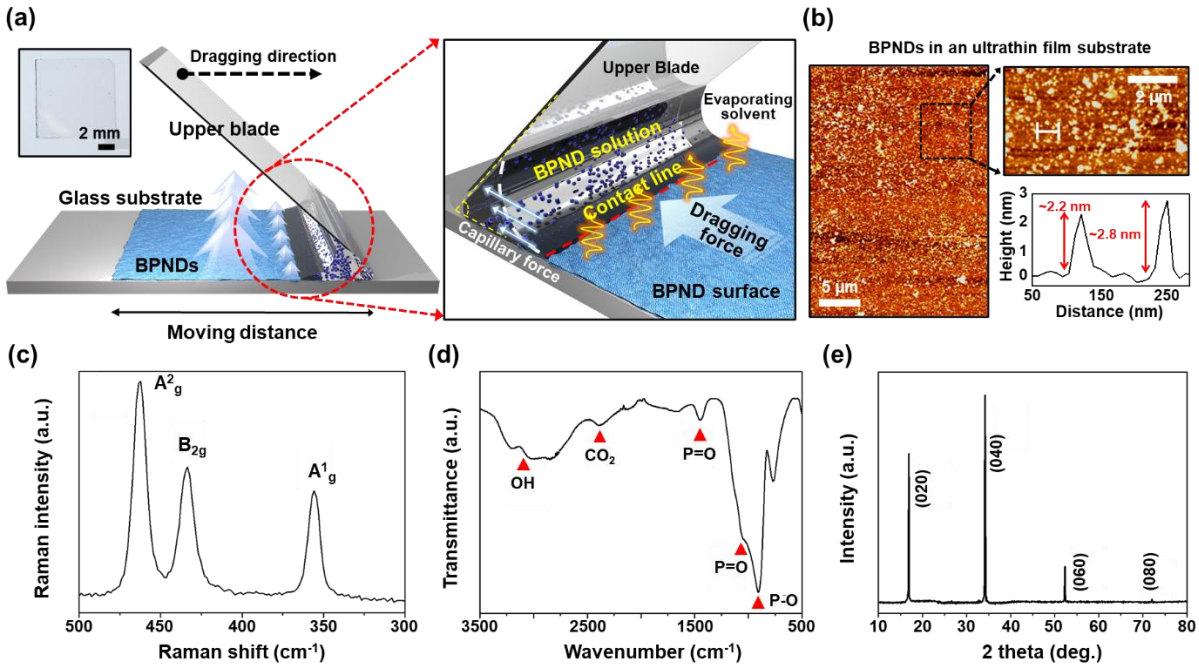

729

730 **Figure 2.** (a) Schematic illustration of the FESA process to produce ultrathin layer of the BPND
731 film on a glass substrate (inset: a digital image of the BPND-coated glass substrate). (b)
732 Representative AFM image with a height profile (lower right panel). Characteristic surface
733 properties of the BPND-coated substrates; Raman spectra (c), FT-IR spectra (d), and XRD
734 peaks (e).

735

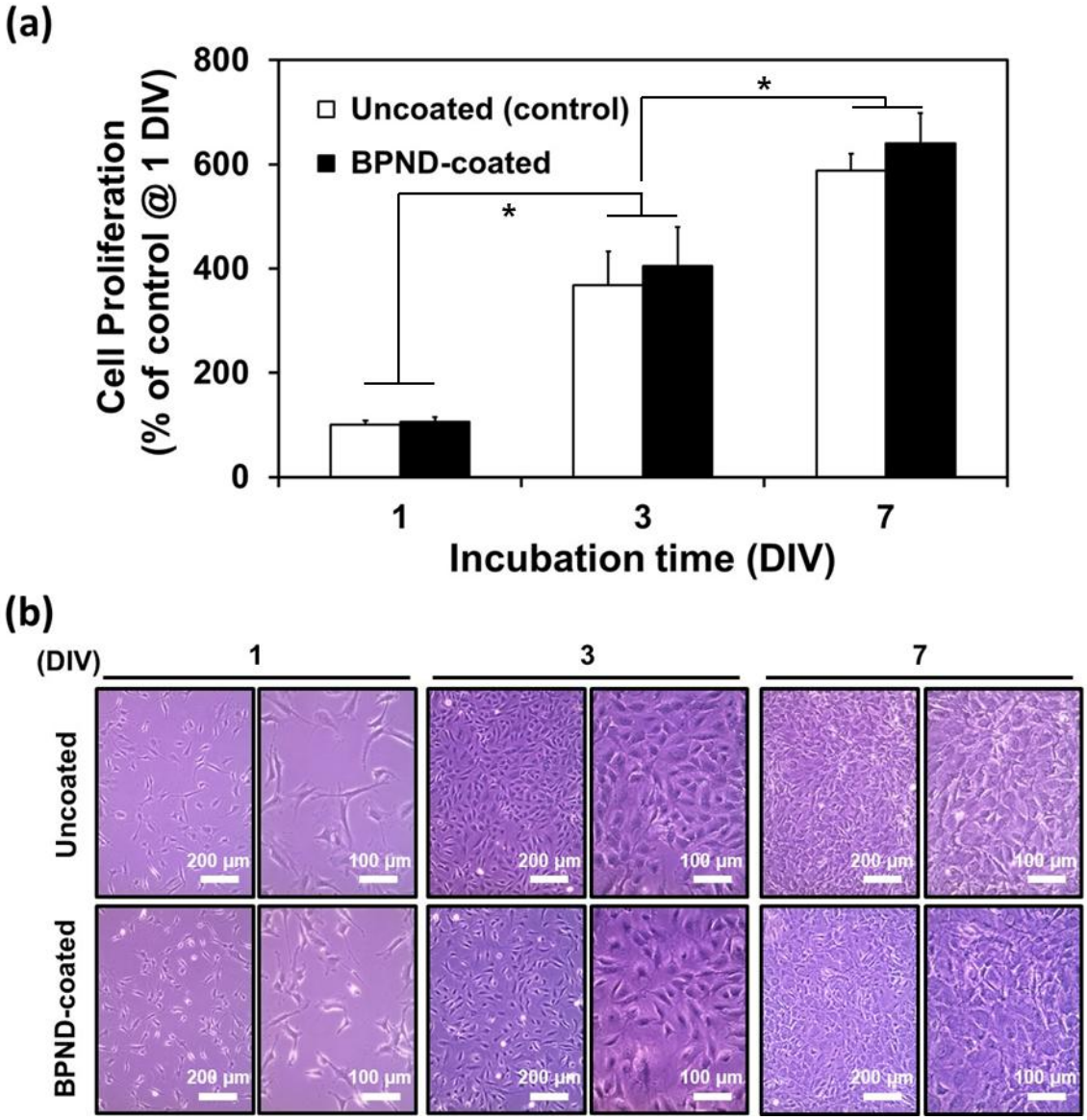

736

737 **Figure 3.** (a) Proliferation of MC3T3-E1 preosteoblasts incubated on uncoated and BPND-
738 coated substrates for 7 days *in vitro* (DIV). The data are expressed as the mean ± SD (n = 6).
739 (b) Cell morphology of MC3T3-E1 preosteoblasts cultured on uncoated and BPND-coated
740 substrates. All micrographs are representative of six independent experiments with similar
741 results. An asterisk (*) denotes a statistically significant difference between the incubation
742 times, $p < 0.05$.

743

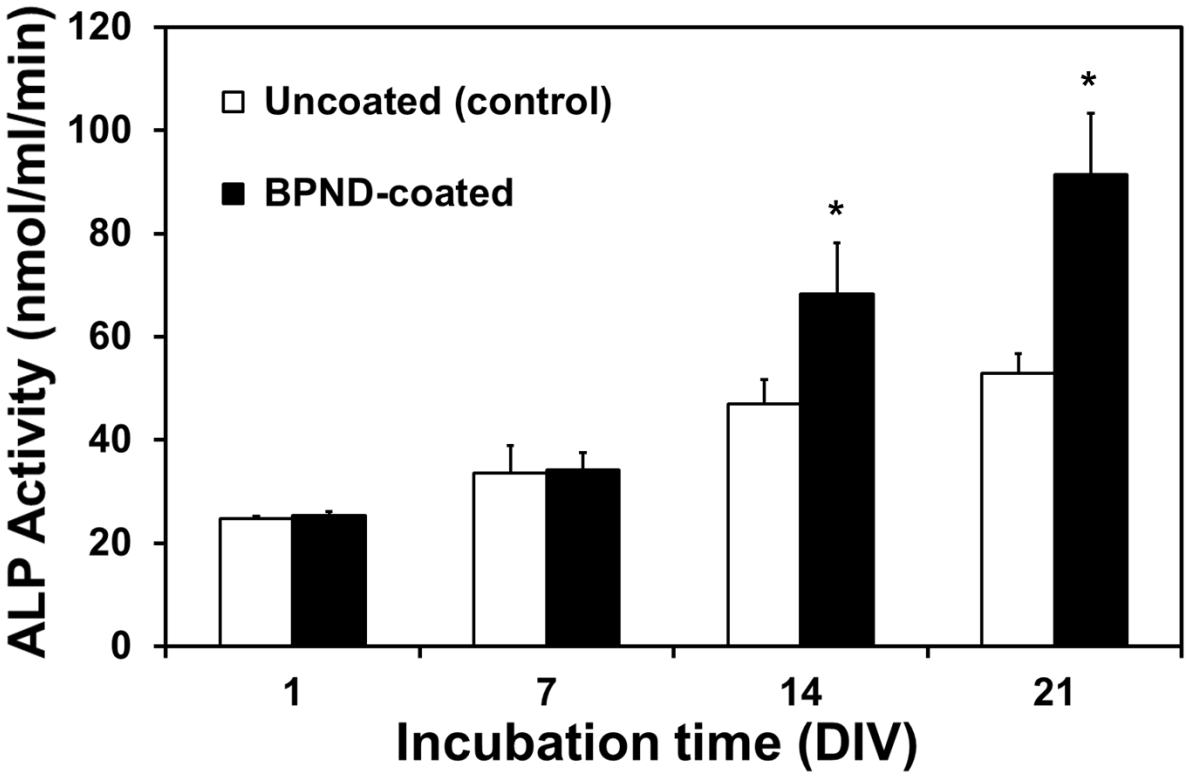

744

745 **Figure 4.** ALP activity of MC3T3-E1 preosteoblasts incubated on uncoated and BPND-coated
746 substrates for 21 DIV *in vitro* (DIV). The data are expressed as the mean ± SD (n = 6). An
747 asterisk (*) denotes a statistically significant difference compared to the uncoated control, $p <$
748 0.05.

749

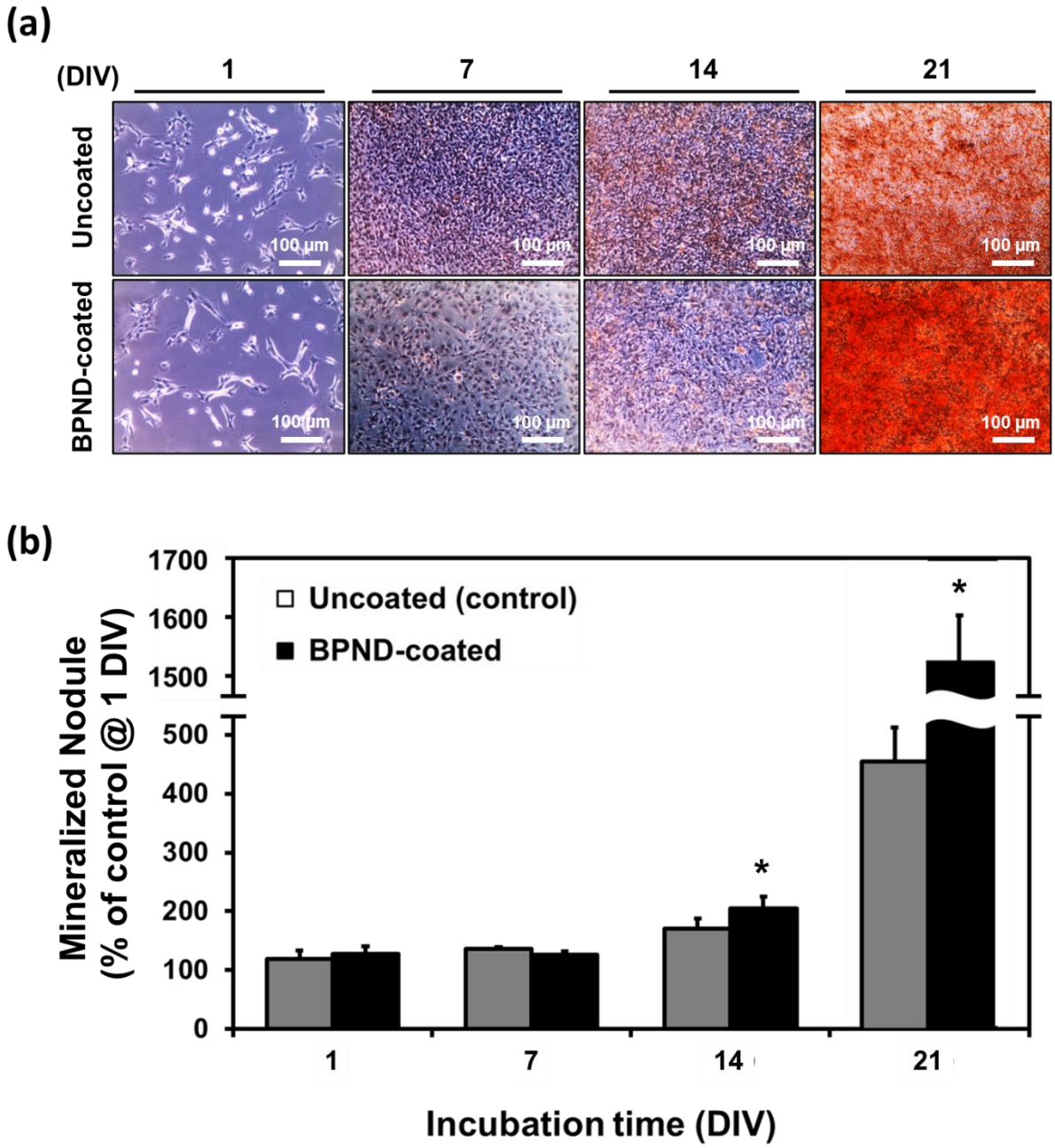

750

751 **Figure 5.** (a) ARS stain and (b) its corresponding extract from MC3T3-E1 preosteoblasts
752 incubated on uncoated and BPND-coated substrates for 21 days *in vitro* (DIV). All micrographs
753 in (a) are representative of six independent experiments with similar results. The data are
754 expressed as the mean ± SD (n = 6). An asterisk (*) denotes a statistically significant difference
755 compared to the uncoated control, $p < 0.05$.

756

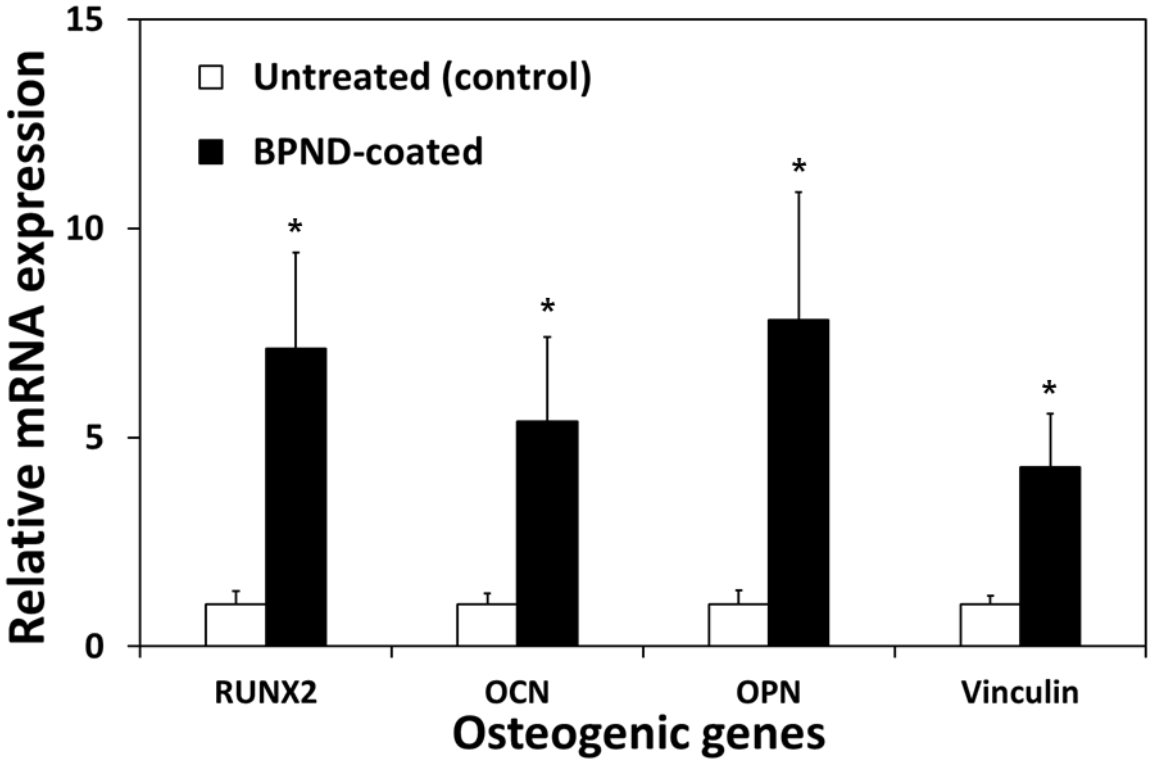

Figure 6. mRNA expression levels of osteogenic markers such as RUNX2, OCN, OPN, and Vinculin in MC3T3-E1 preosteoblasts cultured on uncoated and BPND-coated substrates for 14 days *in vitro* (DIV). All data are presented in the relative amount of mRNA expressed on the uncoated substrate and expressed as the mean ± SD (n = 6). An asterisk (*) denotes a statistically significant difference compared to the uncoated control, $p < 0.05$.

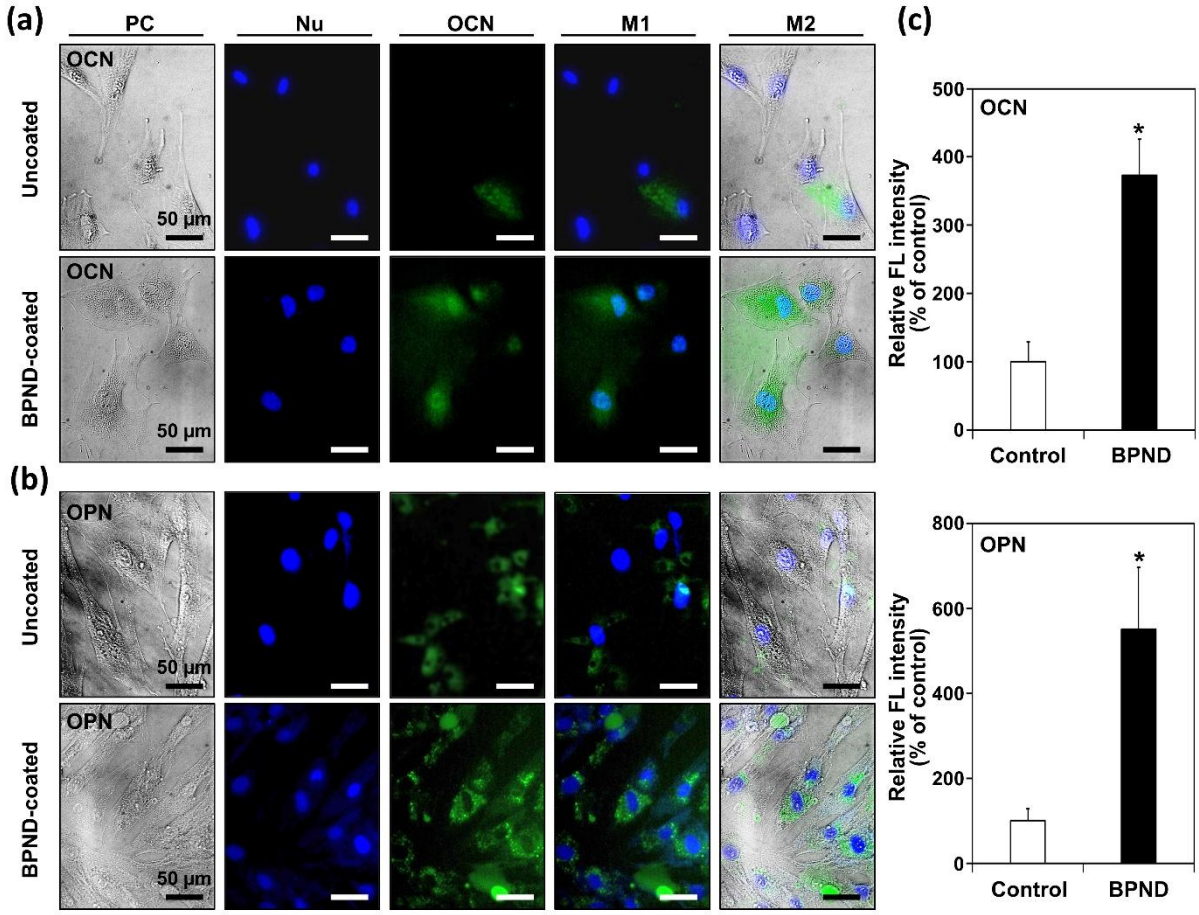

Figure 7. Immunofluorescence staining of OCN (a) and OPN (b) and relative FL intensity (c) in MC3T3-E1 preosteoblasts cultured on uncoated and BPND-coated substrates for 14 days *in vitro* (DIV). All micrographs in (a) and (b) are representative of six independent experiments with similar results (PC: phase contrast, Nu: nucleus, M1: merge of OCN (or OPN) and Nu, M2: merge of PC and M1). All data in (c) are presented in the relative FL intensity on the uncoated substrate and expressed as the mean ± SD (n = 6). An asterisk (*) denotes a statistically significant difference compared to the uncoated control, $p < 0.05$.

Supplementary Information

Spontaneously promoted osteogenic differentiation of MC3T3-E1 preosteoblasts on ultrathin layers of black phosphorus

Sangheon Jeon [a,1], Jong Ho Lee [b,1], Hee Jeong Jang [a,1], Yu Bin Lee [a], Bongju Kim [c], Moon Sung Kang [a], Yong Cheol Shin [d], Dong-Myeong Shin [e], Suck Won Hong [a,*], Dong-Wook Han [a,f,*]

[a] *Department of Cogno-Mechatronics Engineering, College of Nanoscience & Nanotechnology, Pusan National University, Busan 46241, South Korea*

[b] *Daan Korea Corporation, Seoul 06252, South Korea*

[c] *Dental Life Science Research Institute / Innovation Research & Support Center for Dental Science, Seoul National University Dental Hospital, Seoul 03080, South Korea*

[d] *Department of Biomedical Engineering, The University of Texas at Austin, Austin, TX 78712, USA*

[e] *Department of Mechanical Engineering, The University of Hong Kong, Pokfulam 999077, Hong Kong*

[f] *BIO-IT Foundry Technology Institute, Pusan National University, Busan 46241, South Korea*

* Corresponding authors.

E-mail addresses: swhong@pusan.ac.kr (S.W. Hong), nanohan@pusan.ac.kr (D.-W. Han).

[1] contributed equally to the manuscript.

Table S1. qPR-PCR primer sequences for RUNX2, OCN, OPN, Vinculin, and β-actin.

Gene	Forward sequence (5′ → 3′)	Reverse sequence (5′ → 3′)
RUNX2	CACTACCCAGCCACCTTTAC	GGATGCTGACGAAGTACCATAG
OCN	CCAAGCAGGAGGGCAATAA	TCGTCACAAGCAGGGTTAAG
Vinculin	GGCAGAGGTAGTGGAAACTATG	CTCCTGCTGTCTCTCATCAATC
OPN	ACGACGATGATGACGATGATG	GTAGGGACGATTGGAGTGAAAG
β-actin	CGTTCAATACCCCAGCCATG	GACCCCGTCACCAGAGTCC

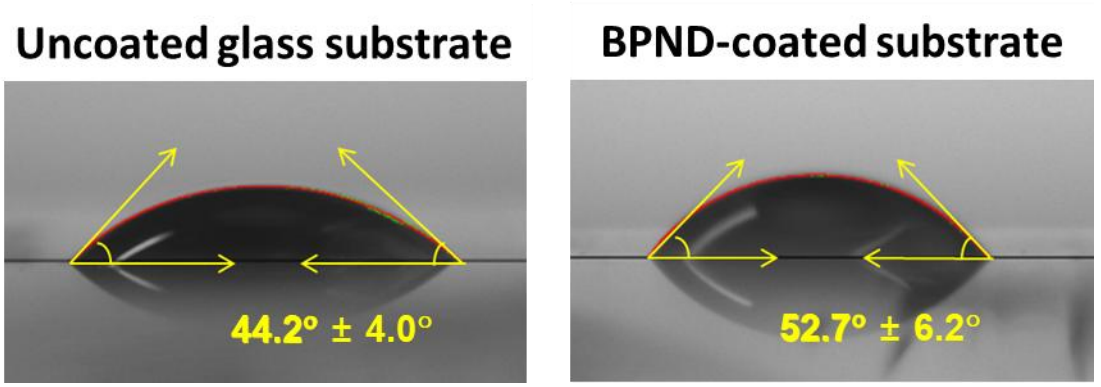

Fig. S1. Water contact angles of uncoated and BPND-coated glass substrates.

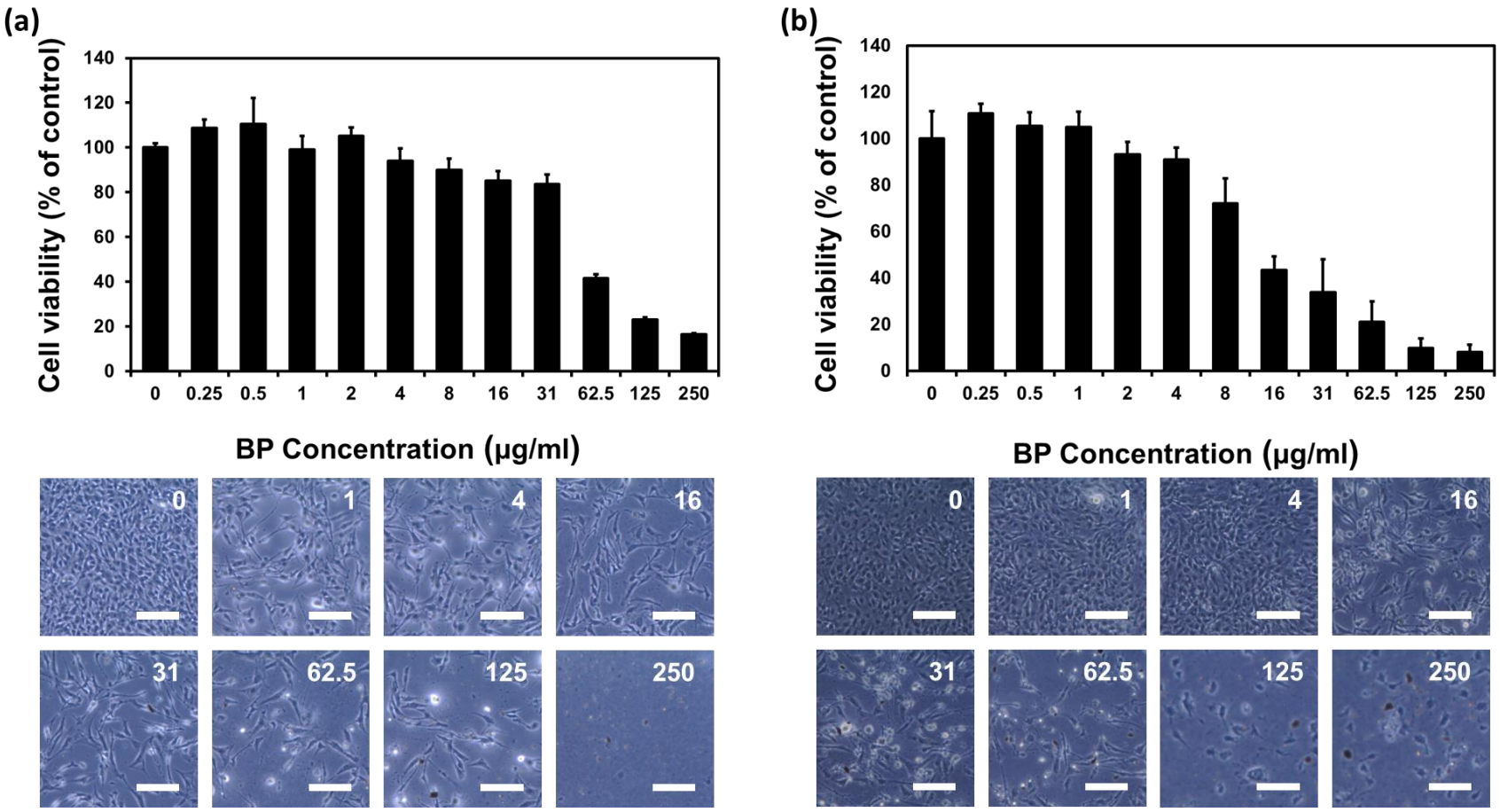

Fig. S2. Cytotoxicity profiles and morphological changes of MC3T3-E1 preosteoblasts after (a) 24 and (b) 48 hours of incubation with increasing concentrations of BPNDs.

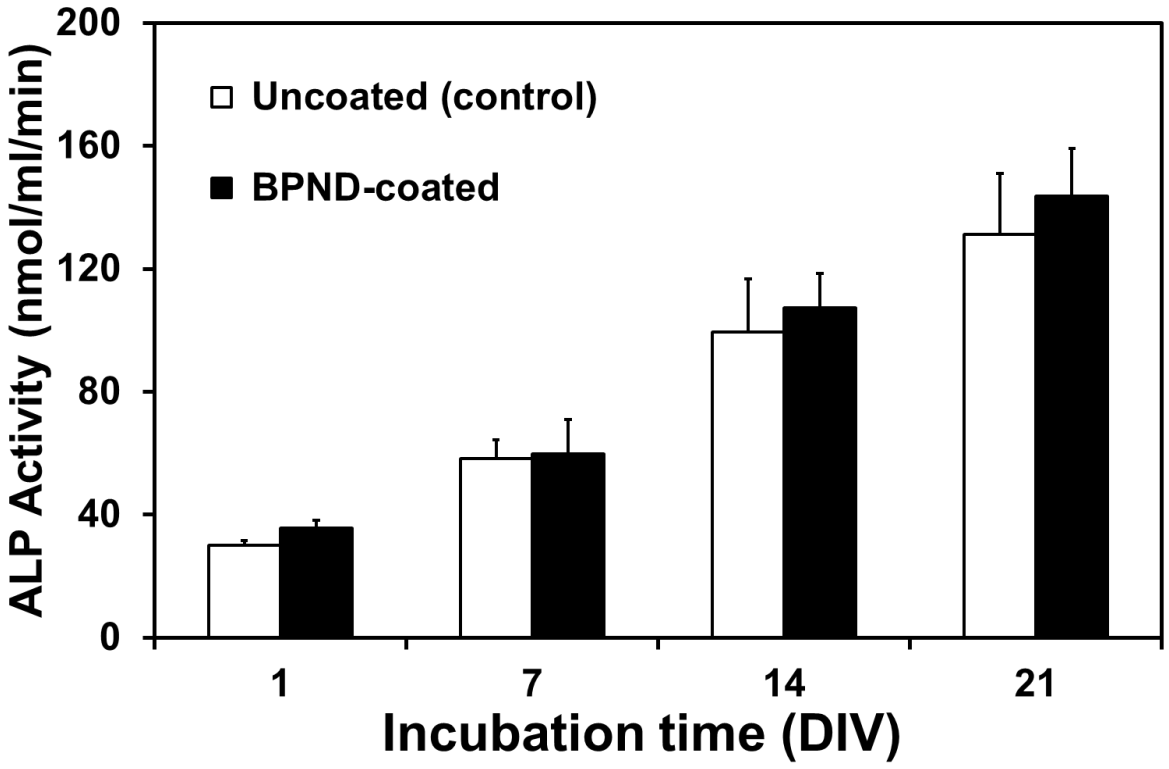

Fig. S3. ALP activity of MC3T3-E1 preosteoblasts incubated on uncoated and BPND-coated substrates in osteoinduction media (OIM) based on α-MEM (basal media) containing 10 mM β-glycerophosphate, 10 nM dexamethasone, and 50 mM L-ascorbic acid for 21 DIV in vitro (DIV). The data are expressed as the mean ± SD (n = 6).